

Spectroscopic Observation of the Stardust Re-Entry in the Near UV with SLIT: Deduction of Surface Temperatures and Plasma Radiation

Michael W. Winterⁱ

*University Affiliated Research Center UARC, UC Santa Cruz
NASA Ames Research Center, Building 230 – Mail Stop 230-3, Moffett Field, CA 94035
Tel.: 1-650-604-1852, Fax: 1-650-604-0350, email: mwinter@ucsc.edu*

and

Kerry A. Trumbleⁱⁱ

*NASA Ames Research Center, Moffett Field, CA, 94035, USA
email: Kerry.A.Trumble@nasa.gov*

Thermal radiation of the heat-shield and the emission of the post-shock layer around the Stardust capsule, during its re-entry, were detected by a NASA-led observation campaign aboard NASA's DC-8 airborne observatory involving teams from several nations. The German SLIT experiment used a conventional spectrometer, in a Czerny-Turner configuration (300 mm focal length and a 600 lines/mm grating), fed by fiber optics, to cover a wavelength range from 324 nm to 456 nm with a pixel resolution of 0.08 nm. The re-entering spacecraft was tracked manually using a camera with a view angle of 20 degrees, and light from the capsule was collected using a small mirror telescope with a view angle of only 0.45 degrees. Data were gathered with a measurement frequency of 5 Hz in a 30-second time interval around the point of maximum heating until the capsule left the field of view. The emission of CN (as a major ablation product), N_2^+ and different atoms were monitored successfully during that time. Due to the nature of the experimental set up, spatial resolution of the radiation field was not possible. Therefore, all measured values represent an integration of radiation from the visible part of the glowing heat shield, and from the plasma in the post-shock region. Further, due to challenges in tracking, not every spectrum gathered contained data. The measured spectra can be split up into two parts: (i) continuum spectra which represent a superposition of the heat shield radiation and the continuum radiation of potential dust particles in the plasma, and (ii) line spectra from the plasma in the shock layer. Planck temperatures (interpreted as the surface temperatures of the Stardust heat shield) were determined assuming either a constant surface temperature, or a temperature distribution deduced from numerical simulation. The constant surface temperatures are in good agreement with numerical simulations, but the peak values at the stagnation point are significantly lower than those in the numerical simulation if a temperature distribution over the surface is assumed. Emission bands of CN and N_2^+ were tracked along the visible trajectory and compared to a spectral simulation with satisfying agreement. Values for the integrated radiation of the transitions of interest for these species were extracted from this comparison.

Nomenclature

A_{SMA}	=	area of the lamp exit
A_{vis}	=	visible SRC surface
c	=	speed of light in vacuum
$corr$	=	correction factor for intensity calibration

ⁱ Research Scientist, Optical Plasma Diagnostics, Member AIAA.

ⁱⁱ Research Scientist, Reacting Flow Environments Branch, Member AIAA.

<i>conv</i>	= conversion factor between incident flux and spectrometer response
D_{tel}	= aperture diameter of the SLIT telescope
f	= focal length, also factor
f/d	= ratio of focal length to diameter
<i>FWHM</i>	= full width at half maximum
h	= Planck's constant: $6.626 \cdot 10^{-34}$ J s
I	= intensity
$l_{lamp-telescope}$	= distance between SLIT-telescope and calibration lamp during calibration measurements
$l_{SRC-DC8}$	= distance between SRC and DC8
k	= Boltzmann constant: $1.3807 \cdot 10^{-23}$ J K ⁻¹
L_{λ}	= spectral irradiance
M_{λ}	= spectral radiance
n_a	= numerical aperture
<i>QE</i>	= quantum efficiency
T	= temperature
T_{Planck}	= temperature for Planck radiation
T_{rot}	= rotational temperature
T_{vib}	= vibrational temperature
α	= apex half angle
ϵ_{λ}	= spectral emissivity
Δv	= change in vibrational quantum number during transition
Φ	= radiant flux
Ω	= solid angle
λ	= wavelength
$\Delta\lambda_i$	= wavelength interval for the filter i
τ	= transmission
Suffixes:	
<i>atm</i>	atmospheric
<i>EM</i>	EMCCD Andor DU971N, CCD camera used during observation
<i>incident</i>	radiation at the DC8 position
<i>i</i>	filter number i
<i>lab</i>	results during recalibration in the IRS lab
<i>obs</i>	results during the observation campaign
<i>OE</i>	open electrode, CCD camera Andor DU920N-OE used during lab experiments for recalibration
<i>pixel</i>	CCD element
<i>scat</i>	scattered light
<i>theory</i>	calibration data provided by the manufacturer
<i>tot</i>	total radiation, i.e. sum of UV and scattered light

I. Introduction

ON January 15th 2006, after a nearly seven-year celestial journey, the Stardust capsule re-entered Earth's atmosphere with a speed of 12.8 km/s.¹ This was the fastest re-entry ever of a human-made space vehicle. Data on heat shield ablation and plasma characterization for this mission would have been very valuable for future sample return missions, e.g., from Mars, which will have similar hyperbolic entry speeds. There were, however, no diagnostics installed in the Stardust capsule to gather data during re-entry. Therefore, the only way to obtain information on the heat shield and re-entry plasma was through passive optical methods, such as the observation mission led by NASA using the Agency's DC-8 airborne observatory.² The observatory was supposed to fly above the clouds at an altitude of 12 km. Absorption in the IR is already rather low at these altitudes, but the ozone layer at altitudes between 25 km and 50 km still anticipates a detection of radiation in the UV (i.e., below a wavelength of 300 nm) due to absorption.

In the observation campaign, a total of 11 different optical experiments were conducted by the American, Japanese and German teams. These experiments were designed to obtain spectrally-resolved data in different wavelength ranges, and with different time resolutions. All spectrally-resolving set-ups used transmission gratings with the exception of a mini Echelle spectrometer,^{3,4} and the German SLIT experiment which had a conventional

spectrometer in a Czerny-Turner configuration ($f=300\text{mm}$, grating 600 l/mm) fed by fiber optics. The spectra contain a superposition of continuum spectra from heat shield radiation and potential dust particles in the plasma,^{5,6} and line spectra from the plasma in the shock layer. The contribution of each of these sources of radiation has to be separated during the data evaluation process. None of the set-ups was able to resolve the emitted radiation spatially. Therefore, all measured data are integrated over the visible part of the glowing heat shield and over the plasma in the post shock region.

In contrast to the other experiments, tracking was a major challenge for the SLIT experiment because the view angle of the telescope was limited to 0.45° to focus on the optical fiber bundle. Data were taken with a measurement frequency of 5 Hz during a 15 s time interval on either side of the point of maximum heating until the capsule left the field of view. Due to difficulties in tracking, not every spectrum contained data. However, the choice of a spectrometer with an entrance slit provided a fixed, and rather accurately determined, wavelength range during the whole observation period. Therefore, besides gathering spectral data with high resolution as far as possible towards the UV, the SLIT experiment was meant to provide some spectral fixed point for the transmission grating measurements.

The strategy for the observation mission included three test flights prior to the re-entry date, primarily to test the different set-ups in flight, and to automate the procedure of mounting the equipment in flight (equipment had to be disassembled during take-off and landing). For the final measurement, the airplane was meant to fly three observation loops (each 15 km wide and 45 km long) at an altitude of 14 km above Nevada,³ such that the third time into the straight part of the loop occurred 90 s before re-entry (the entry interface was defined as an altitude of 130 km of the Stardust capsule). The difficult task of manual tracking the capsule during the observation period was made easier due to excellent work on pre-flight prediction of the capsule's trajectory, and navigation of the observer airplane. All scheduled times were met to within one second by the DC-8 pilots.

In the following, the set-up of the SLIT experiment is described in detail. The evaluation process, including calibration of the measurement and separation of continuum from line spectra, is presented and an interpretation of the measured spectra is given yielding Planck temperatures determined from the measured continuum spectra.

II. Experimental set-up and data acquisition

The SLIT experiment joined the observation campaign rather late in October 2005. Therefore, design, manufacture, and calibration of the whole experimental set up had to be completed within 3 months with only small funding. An Acton 300i spectrometer with a focal length of 300 mm was used. For detection, an Andor DU971N EMCCD camera with 1600×400 pixels of an individual size of $16\times 16\text{ }\mu\text{m}$ was used. The EMCCD technology enables charge from each pixel to be multiplied on the sensor before read out, providing single photon sensitivity with both multi-Megahertz readout and USB connectivity⁷. After trials with different gratings, a 600 l/mm grating was chosen for use in the wavelength range between 324 nm to 456 nm with a pixel resolution of 0.08 nm . Due to instrument broadening, a $FWHM$ of 0.3 nm was obtained in the final measurements.

A reflector telescope was used to focus on the Stardust capsule. Since the useable diameter of the optical fiber was limited by the necessity to feed the radiation into the spectrometer with a small equivalent slit width, the design options for the focusing optics were rather limited. The set up was designed to maximize the view angle under which radiation would be focused on the fiber optics. This constraint required a focal length as small as possible and a fiber diameter as large as possible. On the other hand, the fiber diameter had to be as small as possible to minimize spectral resolution and losses at the entrance of the spectrometer. The f/d ratio of the optics was limited to roughly 2 by the numerical aperture of $n_a=0.22$ of the fiber optics. Finally, an off-axis parabolic mirror with an equivalent focal length of 100 mm and a diameter of 50 mm was chosen. The contradicting requirements for the optic fibers at the telescope and the spectrometer side were resolved using a bundle of 50 fibers with $100\text{ }\mu\text{m}$ diameter each. At the telescope exit they were fixed in a round configuration yielding an overall fiber diameter of 0.6 mm and hence, a view angle of 0.45° (which corresponds approximately to the visible size of the moon). At the spectrometer entrance the fibers were reoriented into a linear row forming an equivalent entrance slit with an effective slit width of less than $100\text{ }\mu\text{m}$. If sufficient light intensity would have been available (which unfortunately was not the case), this slit width could have been further reduced by the mechanical entrance slit of the spectrometer. A spatial assignment of a single fiber in the round cross section to a vertical position in the equivalent slit was not possible due to manufacturing constraints. Therefore, light which hit somewhere in the round cross section was displayed at an arbitrary position on the entrance slit. Since spatial resolution of the Stardust capsule was not possible anyway, for detection, the principle of full vertical binning (FVB) was chosen. Here, all CCD rows are integrated in hardware and are displayed as a single spectrum. The information, which row was carrying the relevant signal is lost but according to the arguments above it did not carry any further information, anyway. Then again, noise is reduced in

general and signal to noise ratio is improved remarkably by this approach. Figure 1 illustrates the combination of telescope, fiber optics and spectrometer and the full vertical binning mode which was used during data acquisition.

Principle design of the SLIT experiment

spectroscopic path with Full Vertical Binning (FVB)

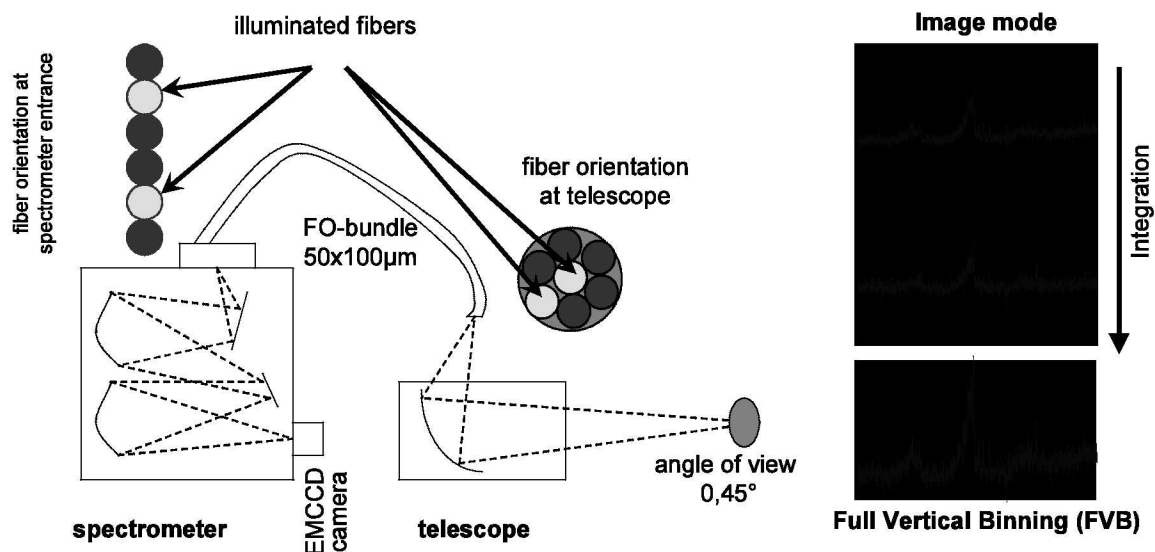


Figure 1. Principle design of the SLIT experiment with an illustration of the full vertical binning mode.

The view angle of 0.45° was far too small to ensure successful manual tracking. Unfortunately, an automatic system with feed-back was not available. Therefore, a conventional video camera was used to tape the screen of a light intensifier with a Canon lens system (focal length 100 mm, $f/2.0$) with a viewing angle of roughly 20° to help with the manual tracking. The intensifier was rigidly connected to the mount of the telescope so that a defined relation between the two viewing angles was granted. Figure 2 shows the combined set-up mounted on a ball mount close to the window of the airplane. A grid was glued to the intensifier screen which enabled an assignment of the detected spot of the spectrometer telescope combination to the video. Figure 3 shows an image of the nightly sky taken during the final observation. The intensifier was strong enough to see the stars in the sky. The constellation Pleiades is clearly seen in the picture. The area detected by the spectrometer is marked by a red dot and was determined using measurements of the moon taken on the tarmac.

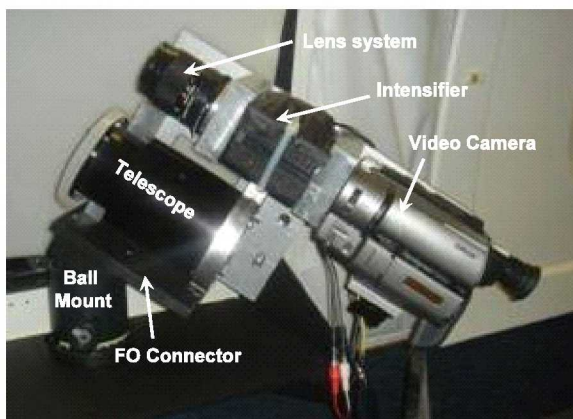


Figure 2. SLIT optics on the ball mount.

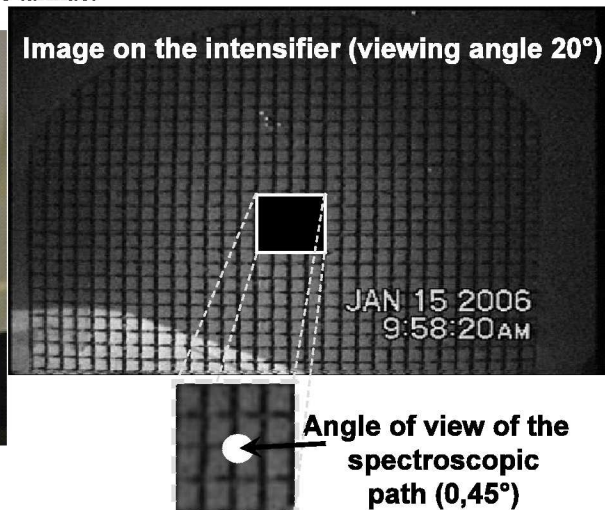


Figure 3. Video image for manual tracking assistance.

During the observation, spectra were taken with an acquisition time of 0.2 s and a repetition frequency of 5 Hz. Even with this set-up, tracking was still rather difficult. It turned out that during data acquisition, not every spectrum contained data because the image of the capsule was not always focused on the optical fiber. Consequently, the overall intensity showed fluctuations, too, when the fiber bundle was only partly illuminated. Only the spectra with the maximal intensity are used for the part of the evaluation that requires absolute intensity information. Although the telescope and the intensifier were rigidly connected to the common base plate, it turned out that the video camera was able to move slightly. Therefore, the point of data acquisition shows slight movements on the video image which was to be taken into account during evaluation. Stardust data was acquired during about 30 s of the re-entry starting at Stardust altitudes of about 84 km over ground down to altitudes of 45 km.

III. Data Correction and Calibration

The data evaluation consists of different steps. In the beginning the raw data have to be corrected for background and cosmic rays. In a second step, the time-correlated data have to be compared with the video image to determine the measurement position (e.g. before, behind or directly on the capsule). The spectral data have to be wavelength corrected and intensity calibrated. Finally, the atmospheric influences (i.e. absorption) have to be taken into account. For this purpose, the horizontal and vertical distances between airplane and Stardust are needed. For the further interpretation of the data, even the orientation of the Stardust capsule relative to the airplane has to be known.

A. Correction for Background and cosmic rays

On the airplane, the occurrence of cosmic rays was significantly higher than on ground. Due to the high sensitivity and amplification of the camera emission lines due to cosmic rays are of intensity comparable to that of true emission lines. Fortunately, these lines appear only on one camera pixel, which is much narrower than plasma emission lines, which are broadened by the optical components to a full width at half maximum of 4 pixels. Therefore, lines due to cosmic rays could be identified and were eliminated from the measured spectra.

The background correction was complicated by a “hot” pixel column at pixel 997 which corresponds to a wavelength of 406.6 nm. After binning and amplification, this column produced a disturbing emission 10 times higher than the highest emission from Stardust. However, a spectrum taken before Stardust was visible could be used as background.⁸

B. Spatial assignment of measured position relative to the SRC

When moving the set up on the track ball, the video camera occasionally moved (slightly) against the base plate where the intensifier and the telescope were mounted. Therefore, a fixed point on the intensifier screen was not always in the same position on the CCD array. A computer routine was developed to apply corrections to compensate for this movement. Groups of pixels were selected for integration and displayed vs. time. The result was compared with the total intensity of the measured spectra, which is simply the sum over all pixels. The best qualitative match between these two curves gives the pixels on the video which correspond to the spot measured by the telescope. Finally, this position can be compared with the image of Stardust on the video and gives spatial information about the measured spot with respect to the SRC (e.g. stagnation point, rear side of the SRC or wake). Figure 4 displays the best match of the integration inside the video and the total intensity on the EMCCD with estimates of the measured position relative to the SRC. Note that a perfect match should not be expected because intensity in the video image is falsified by masking by the grid lines.

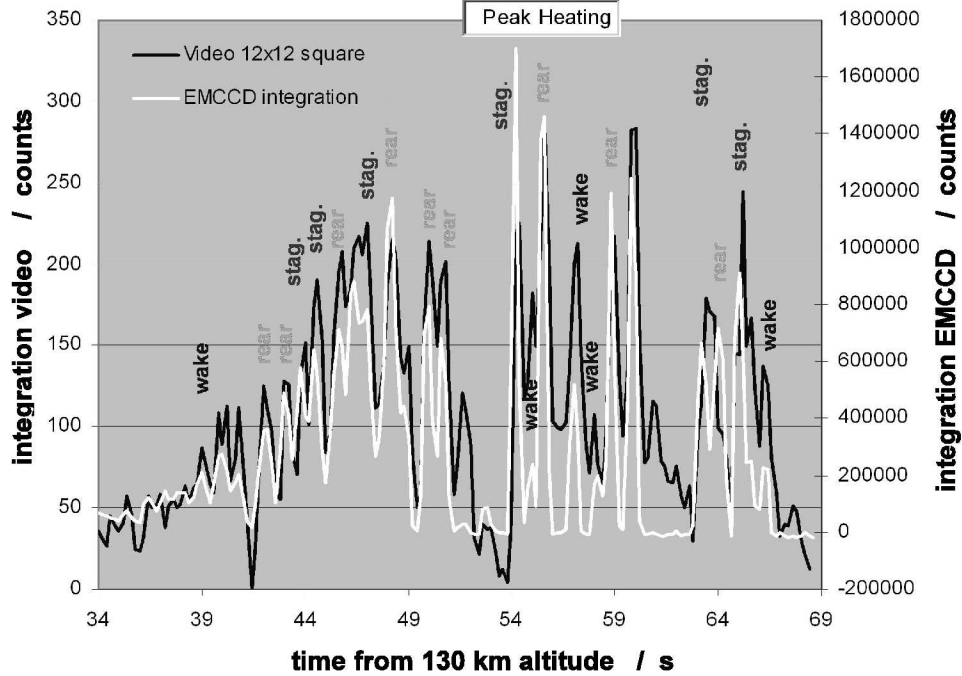


Figure 4. Integration over the measured position in the video image and total intensity on the EMCCD vs. time and estimates of the measured position relative to the SRC. (stag=stagnation point, rear=rear side of the capsule, wake=behind the capsule)

C. Wavelength and Intensity Calibration

Wavelength calibration was performed by measuring the emission of a Mercury lamp. The calibrated wavelengths were then obtained from a second-order polynomial fit. For intensity calibration, a calibration lamp (Ocean Optics LS1) was placed in a distance of $l_{\text{lamp-telescope}} = 3.86 \text{ m}$ to the telescope. The intensity L_{LS1} was given in $\mu\text{W}(\text{cm}^2 \text{ nm})$ for an optical fiber directly connected to the lamp port. This intensity was converted to spectral radiance using the numerical aperture of a typical fiber of $n_a = 0.22$. Obviously, this distance is significantly different from the distance to the Stardust capsule, which varied between 440 km and 70 km during the measurement period in flight. Furthermore, both solid angle and atmospheric transmission varied, too. Therefore, a calibration to radiant power rather than to radiance was carried out. The calibration values were transformed to radiant power at the entrance of the telescope using the distance between lamp and telescope in combination with the telescope aperture diameter. Finally, this value was integrated over the wavelength interval covered by each pixel. During data evaluation, discrepancies between simulated and measured spectra were observed showing inconsistent ratios between the $\Delta\nu=0$ and $\Delta\nu=-1$ bands if the band shape at $\Delta\nu=0$ was correctly reproduced.⁸ This inconsistency pointed to a problem in the calibration. Therefore, recalibration measurements were carried out. It soon became obvious that the calibration was heavily influenced by scattered light inside the spectrometer. The measurement took place in the UV, but the calibration lamp used has its emission maximum between the visible (VIS) and the near infra red (NIR) range. This radiation, which is higher than the UV radiation by at least 3 orders of magnitude, was improperly processed by the spectrometer and appeared at the CCD as scattered light. Figure 5 shows a measurement of a similar calibration lamp (Ocean Optics LS1) with and without an edge filter (Schott GG495) which blocks radiation across the whole measured range. The difference between these measurements gives the lamp emission corrected for scattered light. Unfortunately, the EMCCD camera (Andor DU971N UVB) which was used for the observation mission was not available for the recalibration. Therefore, the recalibration was done with an Andor DU920N OE camera which uses a CCD chip with the same over all dimensions as in the EMCCD. This similarity in dimensions means that the geometrical factors on scattered light are maintained in between the recalibration and the observation. The spectral quantum efficiencies of the two cameras, however, were substantially different as shown in Fig. 5. These manufacturers data were used to extrapolate the scattering results from the one camera to the other.



Figure 5. Calibration lamp Ocean Optics LS1 measured with CCD camera Andor DU920N open electrode with and without edge filter GG495 and quantum efficiencies of the two cameras used.

The amount of scattered radiation is a function of only the spectrometer, the grating and the fiber optics were not changed. In the measured range (i.e. 324 nm to 456 nm) the ratio of the quantum efficiencies was used for conversion. The spectral composition of the scattered light is unknown *a priori*, and varies for different positions on the CCD array (which again correspond to different wavelengths). Therefore, measurements with a series of edge filters (edges at wavelengths 495 nm, 515 nm, 535 nm, 550 nm, 570 nm, 590 nm, 610 nm, 630 nm, 645 nm, 665 nm, 695 nm, 715 nm, 780 nm, 830 nm and 850 nm) were made to estimate the spectral composition of the scattered light from the differences between the single spectra. Above wavelengths of 1000 nm, the sensitivity of both cameras drops down drastically. The main contributions were found to be from radiation between 600 nm and 850 nm.

In the following, the recalibration measurements are referred to by the suffix *lab*, the results with the different cameras are labeled *OE* (open electrode) for the DU920N and *EM* for the DU971N, the measurements during and after the observation are marked by the suffix *obs*. The goal of these measurements was to obtain a scaling factor between measured emission (with and without scattered light) to be applied to the calibration measurements which were taken during the observation campaign. The terms wavelength and pixel do appear simultaneously in some equations to accentuate the pure dependence on wavelength (e.g. the theoretical lamp emission in the UV) and the additional dependence on geometry (i.e. the position on the CCD) where one pixel is affected by radiation from different wavelengths. The measured intensity is the sum of scattered light and UV emission:

$$I_{LS1,tot,lab,OE}(pixel) = I_{LS1,UV,lab,OE}(\lambda) + I_{LS1,tot,lab,OE}(pixel, \Delta\lambda_i) \quad (1)$$

$I_{LS1,UV,lab,OE}$ is a function of wavelength only (and not of geometry), the conversion from the OE (open electrode) camera to the EMCCD of the UV emission is done by a multiplication with the ratio of the quantum efficiencies, which are also functions of wavelength:

$$I_{LS1,UV,lab,EM}(\lambda) = I_{LS1,UV,lab,OE}(\lambda) \frac{QE_{EM}(\lambda)}{QE_{OE}(\lambda)} \quad (2)$$

$I_{LS1,scat,lab,OE}$ depends on geometry and therefore on the pixel position on the CCD and on the true wavelength of the scattered light which is approximated by the combinations of measurements with different edge filters in the wavelength intervals $\Delta\lambda_i$. The contribution of scattered light to the measurement without filter is the sum of all differential measurements with the edge filters, each of them multiplied by the ratio of quantum efficiencies in the wavelength range of concern:

$$I_{LS1,scat,lab,EM}(pixel) = \sum_i I_{LS1,scat,lab,OE}(pixel, \Delta\lambda_i) \frac{QE_{EM}(\Delta\lambda_i)}{QE_{OE}(\Delta\lambda_i)} \quad (3)$$

The desired relation is then:

$$f_{LS1,UV,EM}(pixel) = \frac{I_{LS1,UV,lab,EM}(\lambda)}{I_{LS1,UV,lab,EM}(\lambda) + I_{LS1,scat,lab,EM}(pixel)} \quad (4)$$

If $f_{UV,EMCCD}$ is multiplied with the measured emission of the LS1 lamp during observation the results should be the true emission in the UV range:

$$I_{LS1,UV,obs,EM}(\lambda) = f_{LS1,UV,EM}(pixel) I_{LS1,tot,obs,EM}(pixel) \quad (5)$$

If applied to the calibration measurement during the observation, the reconstruction using the above ratios does only match the measured emission below 400nm if the scattered light is increased by 35%. For reasons unknown,

the amount of scattering seemed to have changed during the observation and the recalibration. Since no reasonable explanation can be given for this effect, all following analyses have been performed both with the original values for scattered light from the lab measurements and with a value increased by 35%, to get an idea of the errors introduced by this variation. As will be shown later, the effect on the Planck temperatures to fit the measured data is rather small due to the shape of the Planck curve. For calibration of the true UV radiation, the ratio of the UV portion of the calibration measurement and the calibrated radiance of the lamp $L_{LSI, theory}$ provided by the manufacturer is used. For the plasma spectra, the effect of scattered light from plasma emission in the VIS and NIR would be in the noise level of the measured data if the plasma emission is lower than the thermal radiation by one order of magnitude. Therefore this effect is considered negligible. Following the procedure described at the beginning of this section, the original calibration curve was converted from the calibration units $[\mu W/cm^2 nm]$ to an incident radiant power in $[\mu W]$ by:

$$\Phi_{LSI,incident}(\lambda) = L_{\lambda,LSI,theory}(\lambda) A_{SMA} \frac{\Omega_{tel}}{\Omega_{el}} \Delta\lambda_{pixel} \quad (6)$$

with: A_{SMA} : area of the lamp exit

Ω_{LSI} : solid angle in which the lamp radiation is emitted, determined from the numerical aperture $n_a = 0.22$ given by the manufacturer.

Ω_{tel} : solid angle from which the telescope receives radiation, determined from the geometry

$\Delta\lambda_{pixel}$: wavelength width of each pixel.

A correction factor is obtained to:

$$corr_{LSI,UV,EM}(pixel) = \frac{\Phi_{LSI,incident}(\lambda)}{I_{LSI,UV,obs,EM}(\lambda)} \quad (7)$$

Figure 6 shows the obtained calibration factors with and without correction for scattered light as well as the calibrated curve provided by Ocean Optics. This calibration curve combined with the atmospheric extinction was used for the calibration of the plasma spectra.

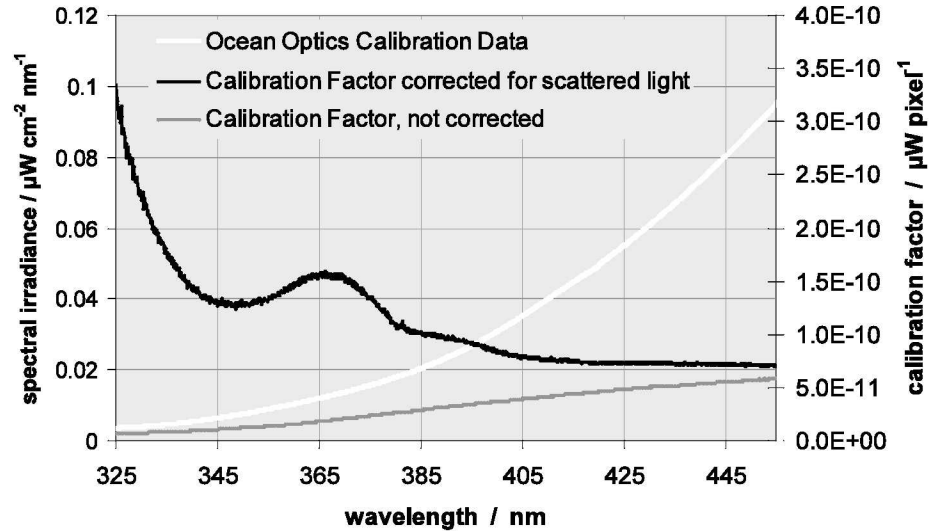


Figure 6. Ocean Optics calibration data and SLIT calibration factor.

Since the thermal emission of the glowing heat shield is grey body radiation, it shows very similar ratios in the different wavelength ranges as the calibration lamp. Consequently, these measurements too are contaminated by scattered light. The amount of scattered light depends on the spectral distribution in the VIS and NIR range, which varies with the underlying surface temperature. Therefore, the factors for scattered light will change with SRC surface temperature. As a consequence of this variation, separate determination of scattered light had to be performed for each single spectrum. A uniform calibration was not possible for the thermal radiation since the underlying Planck temperatures were not known. Rather than converting the measured signal to radiant power, the simulated Planck emission of the SRC surface was converted to counts measured by the spectrometer system giving a simulated spectrometer response to any assumed Planck radiation including the effects of scattered light. Again,

the measurements of the LS1 calibration lamp with the edge filter combinations were used. For each wavelength interval $\Delta\lambda_i$, the product of the calibrated intensity $L_{\lambda,LS1,theory}$ in $[\mu W/cm^2 nm]$ provided by the manufacturer and the combined transmission of the filter combination of concern was integrated over wavelength:

$$L_{LS1,theory}(\Delta\lambda_i) = \int L_{\lambda,LS1,theory}(\lambda) \{t_i(\lambda) - t_{i-1}(\lambda)\} d\lambda \quad (8)$$

and converted to incident radiant power $\Phi_{LS1,incident,obs}(\Delta\lambda_i)$ as described above. For the UV radiation, the correction factor for intensity calibration is inverted. Thus, conversion factors are obtained to:

$$conv_{theory,scat,obs}(pixel, \Delta\lambda_i) = \frac{I_{LS1,scat,obs,EM}(pixel, \Delta\lambda_i)}{\Phi_{LS1,incident,obs}(\Delta\lambda_i)} \quad (9)$$

$$conv_{theory,obs}(\lambda) = \frac{1}{corr_{LS1UV,EM}(pixel)} = \frac{I_{LS1UV,obs,EM}(\lambda)}{\Phi_{LS1,incident}(\lambda)} \quad (10)$$

in $[counts/\mu W]$

These conversion factors are used to transform incident radiant powers into a simulated spectrometer signal. To account for the observed uncertainty in the amount of scattered light, all analyses are conducted both for the above shown value and the one increased by 35%. For the following analysis of the measured spectra, thermal radiation emitted by the SRC heat shield at a given temperature is computed and corrected for distance, solid angle, SRC orientation (i.e. effective emitting area) and atmospheric extinction until an incident thermal radiation at the telescope position is received. This incident thermal radiation is converted into an equivalent spectrometer response and compared to the measured raw data. The underlying Planck temperature distribution for the best fitting spectrum is considered as the desired solution. The plasma spectrum is then extracted as the difference between measured spectrum and simulated response to the best fitting Planck radiation. In the following, the different influences on the SRC radiation will be discussed and the method of generating the simulated thermal radiation will be shown.

D. Atmospheric Transmission

For a conversion of radiation emitted by Stardust (i.e., Planck and plasma radiation) it must be multiplied with the corresponding solid angle obtained from the distance, the emitting surface area or plasma volume and with the corresponding air transmission. The spectral transmission of the atmosphere was computed using the ModTran code^{9,10} using aerosol and ozone concentration as input parameters. Assuming aerosol concentration to be “normal,” ozone concentration was determined to 300 DU (Dobson Units) from ozone maps from the *World Ozone and Ultraviolet Radiation Data Centre* provided by the Environment Canada on the internet for the re-entry day of Stardust.

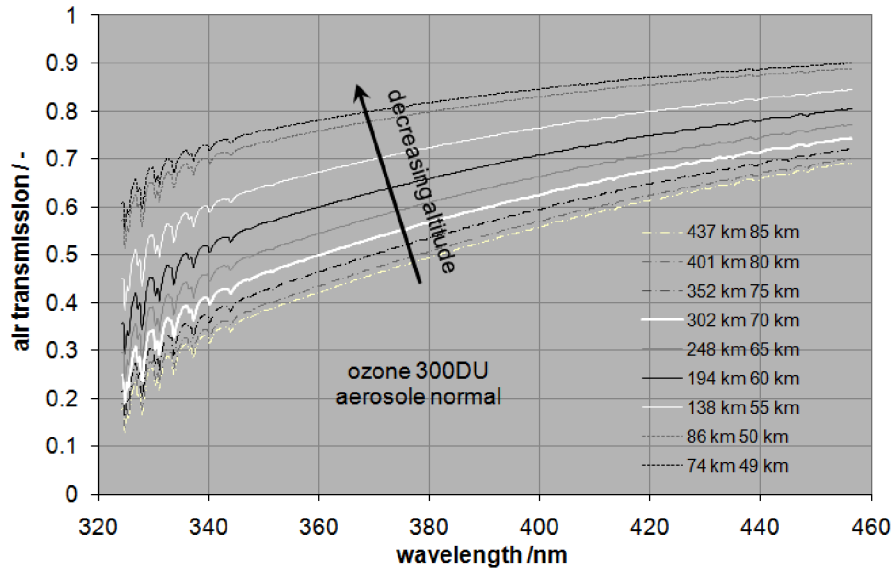


Figure 7. Atmospheric transmission between DC8 and Stardust for different Stardust altitudes.

IV. Simulation of the Stardust Re-entry

A. Flow Field

The method of analysis for the thermal protection system begins with computation of the flow field at several time points (to sufficiently capture the heat pulse) along the estimated flight trajectory (EFT). For the present work, flow fields solutions along the EFT were calculated using the computational fluid dynamics (CFD) code DPLR (Data Parallel Line Relaxation). DPLR is a parallel, multiblock, finite-volume code that solves equations governing the continuum flow of a mixture of gases in chemical and thermal nonequilibrium. The Euler fluxes are computed using modified Steger-Warming flux vector splitting¹¹ with third-order spatial accuracy via MUSCL extrapolation.¹² The viscous fluxes are computed to second-order accuracy using a central-difference approach. The flow is assumed laminar, in thermochemical nonequilibrium, and is modeled with a two-temperature, 11 species (N_2 , O_2 , NO , NO^+ , N_2^+ , O_2^+ , N , O , N^+ , O^+ , and e^-) and 19 reactions finite-rate air chemistry model. Vibrational relaxation is based on the Landau-Teller formulation; relaxation times are obtained from Millikan and White,¹³ assuming a simple harmonic oscillator model, with the high-temperature correction of Park.¹⁴ Rotational relaxation is based on the Parker model.¹⁵ Viscous transport and thermal conductivity are determined using the mixing rules of Gupta et al.¹⁶ The species diffusion coefficients are calculated with a bifurcation model,¹⁷ which has been shown to compare well with exact solutions of Stefan-Boltzmann equations.¹⁸ The surface of the heat shield is assumed to be in radiative equilibrium with a constant emissivity of 0.85. Furthermore, the wall is assumed fully catalytic with a catalytic efficiency of 1.0 for atom recombination; the wall was assumed fully catalytic to ions as well.

Since Stardust is an axisymmetric configuration, and its entry trajectory was ballistic,¹⁹ flow field analyses can be performed using a two-dimensional axisymmetric grid, thereby saving computational resources. The grid used in the present work was composed of six blocks and 43,000 grid cells. The grid was grown out hyperbolically in the body-normal direction and orthogonality of grid lines at the surface was ensured. As the solution converged on the hyperbolic grid, the grid was then tailored to achieve good alignment of the outer boundary with the bow shock.

Since high-fidelity CFD computations are performed only at a finite number of time points on the EFT, aerothermal environments along the entire trajectory are constructed using a combination of CFD and engineering scaling relationships. Between CFD solutions, environments are linearly interpolated in time using the CFD results. At trajectory points outside the time interval considered for CFD, aerothermal environments are determined using scaling relations based on freestream velocity and density (i.e. enthalpy scales with v^2 , heat transfer coefficient scales with $[\rho v]$, pressure scales with $[\rho v^2]$). Scaling will vary spatially over the heat shield. Therefore, each surface point is scaled separately to provide heating pulse continuity in time.

B. Material Response

In the present analysis, PICA material response along the Stardust EFT is modeled using version 2.4 of FIAT,²⁰ and Version 3.3 of the PICA model.²¹ The aerothermal environment (recovery enthalpy, pressure and heat transfer coefficient) along the trajectory, as determined from CFD simulations is input into FIAT. In the present analysis, the contribution of shock-layer radiation is not included since it accounted for less than 10% of the heat rate at peak heating, and surface heating was dominated by convective heating.²² Next, the surface energy balance equation that accounts for conduction, blowing, pyrolysis and surface recession is solved. The material stack consists of PICA (5.8 cm), HT-424 (0.14 cm) and aluminum 2024 (1.27cm) and a planar geometry is employed. All materials have an assumed initial temperature of -20 °C. There is no contact resistance at any material interface and the back wall is assumed adiabatic. The properties (heat capacity, thermal conductivity, emissivity) of the material in the TPS stack are read in from the FIAT material database. Heat capacity is modeled as a temperature dependent quantity, while thermal conductivity varies with both pressure and temperature. For ablators, these material properties are separately listed for virgin and char material. Within FIAT, the emissivity of PICA for both virgin and char is modeled as temperature dependent and varies from 0.858 at 250K to 0.93 at 3500K.

The iteration between CFD and FIAT is loosely coupled—the surface temperatures returned by FIAT are put back as a point-by-point isothermal boundary condition into the DPLR CFD code, and a flowfield solution is recomputed. This loosely-coupled iterative procedure is deemed converged when the differences in heat fluxes from two successive cycles of DPLR-FIAT iterations are within 5% based on Olynick's work.²³

V. Data Evaluation and Interpretation

Measured spectra are a superposition of shock-layer radiation, and continuous radiation emitted by the glowing heat shield. As a first step, both plasma parameters and heat shield temperature are assumed constant. In reality, this assumption is tenuous because temperature varies across the surface of the heat shield, as do the plasma composition and temperatures across the shock layer. Therefore, in a second step, a surface temperature distribution based on CFD simulations is used. It should be noted that the ablation process most likely causes particles to be injected into the flow. These material particles themselves emit continuum radiation due to their surface temperature.^{5,6} However, without any further information about the size and loading of the particles in the shock layer nothing further can be done because there are too many free parameters to obtain a single solution. Possible improvements of the evaluation procedure to relax these restrictive simplifications are discussed later. Regardless, the plasma (or shock-layer) radiation and the Planck (or capsule surface) radiation have to be separated as a first step. To quantify the Planck radiation, the visible surface of the Stardust capsule and the distribution of the angle between the surface normal vector and the optical axis to the DC8 must be known for each surface element. If a constant surface temperature is assumed the individual factors can be summarized to a single viewing factor.

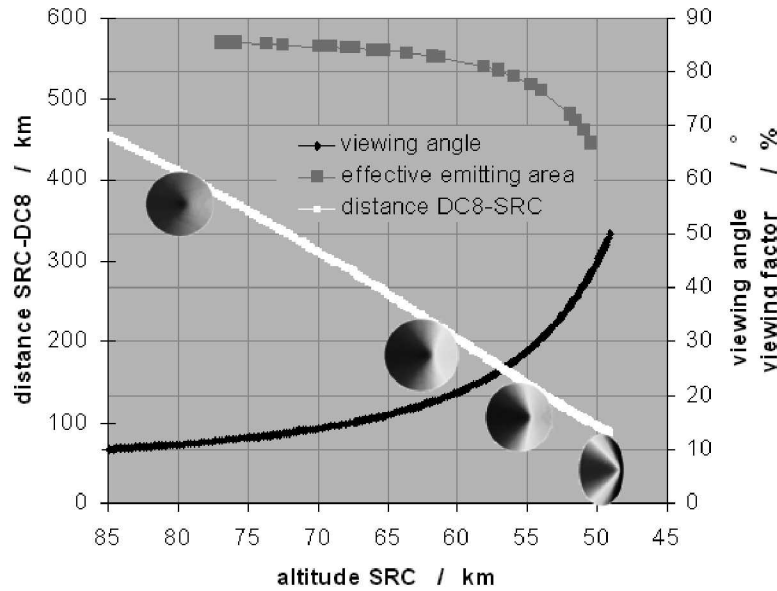


Figure 8. Distance SRC-DC8*, viewing angle* and averaged viewing factor vs. SRC altitude (*: according to Nominal Entry Trajectory Data: s06015f,¹⁹ **: this work).**

A. Visible Surface and Viewing Factors

The position and orientation of the DC8 observation aircraft are known from GPS data, and the Stardust capsule position is taken from the trajectory data. For the orientation of the Stardust capsule it is assumed that the vehicle axis is oriented in direction of the velocity vector which is extracted for each altitude from the difference of two successive trajectory points. If these data sets are combined, the distances and view angles as depicted in Figure 8 are obtained. The view angle is defined to be 90° if the observation axis coincides with the vehicle axis (view from the front), and 0° if the vehicle is observed at right angles to the flight vector (side view). The minimal angle during the observation period was 34.33° at an altitude of 48.5 km. The surface has been calculated as a sphere with a radius of 0.22 m up to an angle of 30.5° and a truncated cone with a cone angle of 30.5° up to an outer radius of 0.405 m. Due to this shape of the Stardust capsule, the whole heat shield surface of 0.5947 m² is completely visible down to a minimum angle of 30.5°. However, according to Lambert's Law the detected intensity of a radiating surface is proportional to the cosine of the angle under which the surface is observed. Therefore, the detected intensities decrease with this angle, thereby yielding an increase in the deduced Planck temperature. This effect is covered by the view factor. For the assumption of a constant surface temperature, integration over the whole surface yields an average view factor for each altitude as depicted in Fig. 8. If a temperature distribution is applied, the

integration has to be done over the product of locally emitted Planck radiation with the local viewing factor at each surface position. Images of the SRC in its orientation to the DC8 are added to Fig. 8.

B. Estimation of Heat Shield Temperatures

Two cases (a) of constant SRC surface temperature over the heat shield for the entire flight trajectory, and (b) a predefined temperature distribution (piecewise linear variation) are investigated in parallel. Both cases are best considered approximations because of these simplifying assumptions. For the second case the “real” distribution is approximated as a combination of two linear distributions. The shape of this combination was obtained from an analysis of temperature distributions from CFD simulations using DPLR. For this purpose, all CFD-predicted temperatures are normalized the value at the apex of the heat shield (also the stagnation point), and normalized CFD distribution is approximated by two straight lines which intersect at an axial location of 5 cm approximately from the apex. This distribution matches the CFD solution on the spherical part of the heat shield close where the highest surface temperatures (consequently the highest contribution to thermal radiation) are predicted. However, the distribution does show deviations at larger distances from the tip. At this part of the surface, the simplified distribution over predicts the DPLR temperatures at high altitudes and under predicts them at lower altitudes. If the same radiative flux has to be reproduced this would yield lower experimental temperatures at early re-entry and higher values at the end of the observation period. Note that only the shape of the distribution is adapted from DPLR solutions. No temperature values are interchanged, thus keeping the data analysis independent of the CFD solution. For the analysis, the SRC tip temperature was varied and the temperatures across the surface were computed according to this approximation, assuming rotational symmetry. Figure 9 shows the assumed temperature distribution in comparison to the normalized DPLR results. A consistency check between the two cases of constant and varying surface temperature to prove the integration procedure over the surface has been performed by reproducing the thermal emission for a constant surface temperature if a flat line with corresponding temperature was chosen as input.

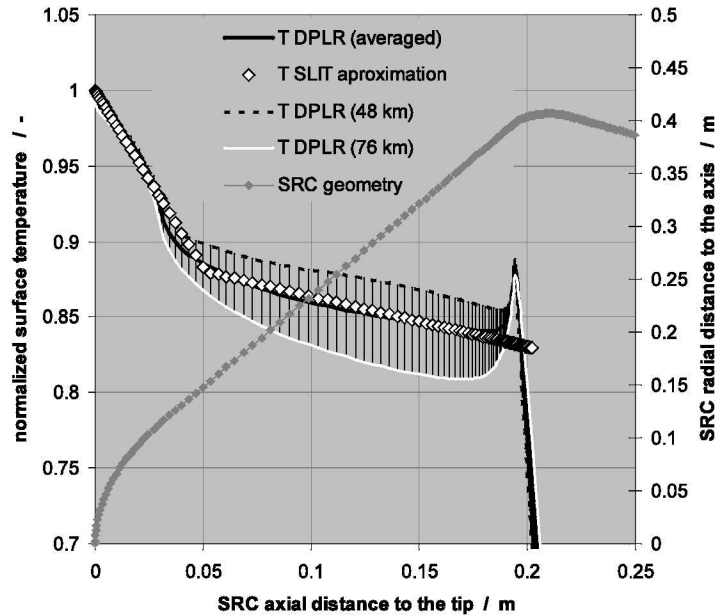


Figure 9. Assumed SRC temperature distribution in comparison to normalized DPLR results.

Spectral radiance from the glowing heat shield was calculated according to Planck’s formula for a grey body:

$$M_{\lambda}(T) = \varepsilon_{\lambda} \frac{2\pi hc^2}{\lambda^5} \frac{1}{\exp\left(\frac{hc}{\lambda kT}\right) - 1} \quad (11)$$

The emissivity of PICA is assumed independent of wavelength since no such spectral data are available. Temperature dependent emissivity data for PICA after arc jet testing are available only for temperatures below 1900 K.²⁴ Above 1920 K the emissivity is assumed to be constantly 0.9.

The spectral radiance was first integrated to the wavelength widths of the different CCD pixels and then multiplied by the visible surface area, the atmospheric transmission already shown in Fig. 7, and the solid angle:

$$\Omega = 2\pi(1 - \cos \alpha) \quad (12)$$

where the apex half angle

$$\frac{\alpha}{2} = \arctan\left(\frac{D_{tel}}{2L_{SRC-DC8}}\right) \quad (13)$$

is given by the aperture diameter of the telescope D_{tel} and the distance between Stardust and DC8 $L_{SRC-DC8}$. Thus, the radiant power Φ at the entrance aperture of the telescope was obtained as:

$$\Phi = \int_{\Delta\lambda_{pixel}} M_{\lambda} \Omega A_{vis} \tau_{atm} d\lambda \approx M_{\lambda} \Omega A_{vis} \tau_{atm} \Delta\lambda_{pixel} \quad (14)$$

The surface temperatures were systematically varied and the emitted radiation was integrated over the whole surface area taking into account the viewing angle given by the relative positions of DC8 and SRC along the trajectory and multiplied with the solid angle for detection and with the air transmission determined with a ModTran calculation as already shown in Fig. 7 and finally divided by the window transmission of 0.93. Thus, a radiant power at the entrance of the telescope was achieved.

Since emission by particles inside the post shock layer is not taken under consideration, these peak temperatures are presently considered to be an upper limit. Inclusion of particle radiation in the analysis will require specification of additional free parameters such as particle size, penetration depth into the boundary layer, particle surface temperature, etc.; these parameters are not known with certainty. Therefore, an implementation of this mechanism at the level of analysis presented here is not useful. For future investigation, it is recommended to further investigate the ablation process in ground test facilities as done in Ref. 5 with particular respect to spallation to obtain further information about these parameters.

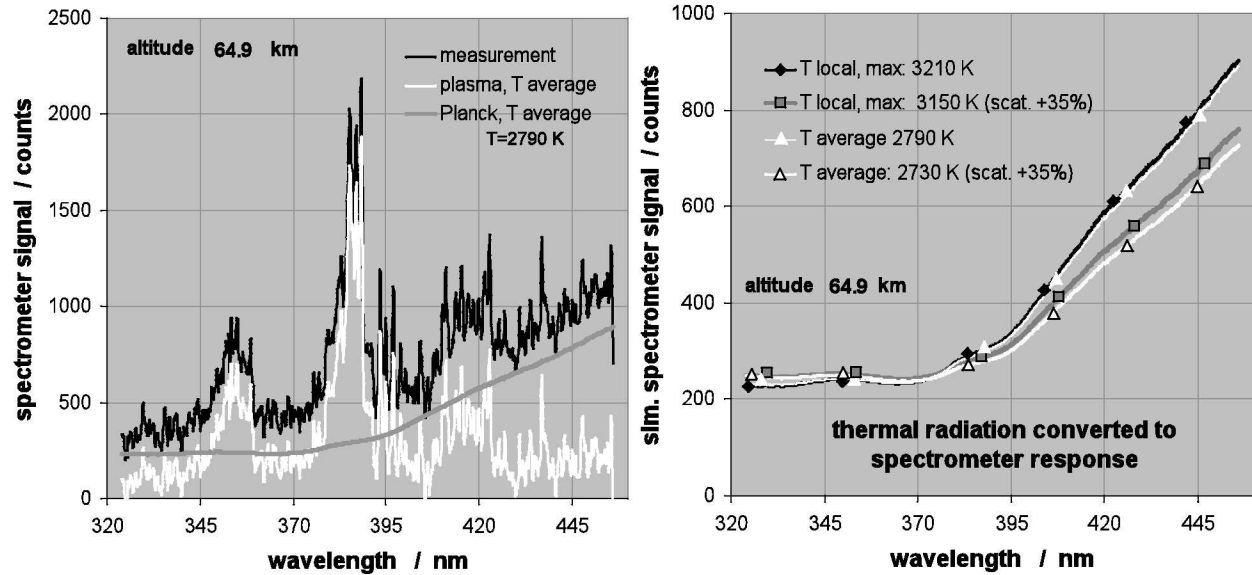


Figure 10. Measured spectrum, split up into Planck- and plasma-components, for an SRC altitude of 64.9 km close to peak heating and comparison of the spectrometer response to thermal radiation for average and local surface temperatures with and without enhancement of scattered light by 35%.

Figure 10 shows an example for the measured spectrum from the SRC at an altitude of 64.9 km. This spectrum is the most reliable one close to peak heating. Furthermore, the best fitting Planck radiation and the resulting plasma spectrum (which is the difference between measurement and Planck) are displayed. As discussed earlier, discrepancies between calibration during the observation and recalibration in the ground laboratory due to scattered light below 400 nm remain to be reconciled. Therefore, results with unmodified and enhanced scattering are processed in parallel. The results are shown in the right hand part of Fig. 10. With scattering enhanced by 35% a slightly lower surface temperature is obtained, but the maximum difference does not exceed 60 K. Since the

qualitative agreement with the measured spectra is slightly better without enhancement of scattered light, the following results are based on the spectrometer response with unmodified scattered light. Surprisingly, the spectral shape of the spectrometer response for constant surface temperatures and the temperature distribution is nearly the same in the wavelength range of interest.

The plasma spectrum extracted from this comparison is now calibrated with the correction factor shown in Fig. 6. The total radiation is computed as the sum of calibrated plasma spectrum and simulated thermal radiation without influences of scattered light as shown in Fig. 11 at an altitude of 64.9 km in units of radiant flux through the aperture of the telescope.

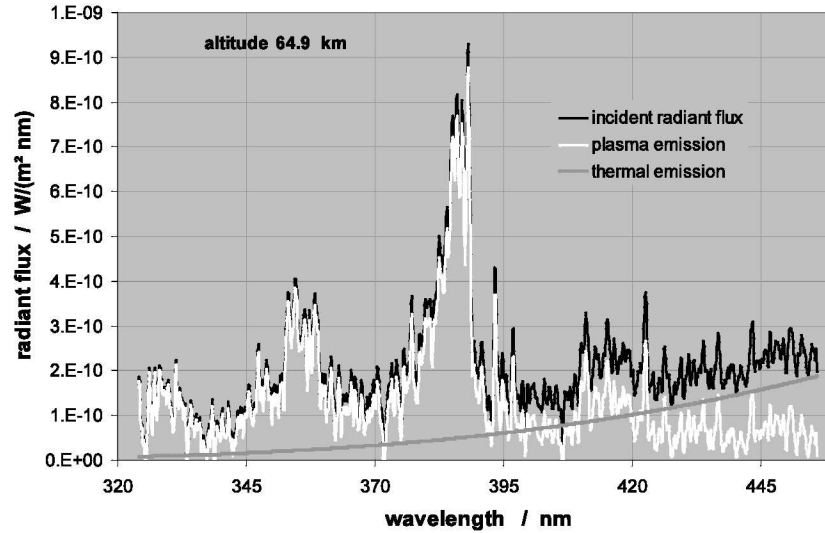


Figure 11. Emission spectrum at the DC-8 position as combination of thermal radiation of the Stardust heat shield and plasma emission at an altitude of 64.9 km after calibration.

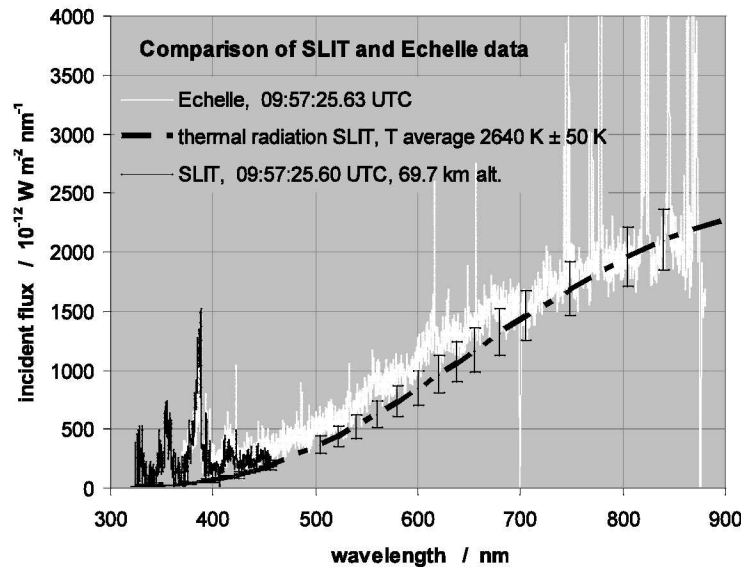


Figure 12. Comparison of the SLIT spectrum and an extrapolation of the extracted thermal emission to the NIR/VIS with an Echelle spectrum²⁶ at an altitude of 69.7 km.

The results are in good agreement with those obtained by the ASTRO²⁵ and the Echelle²⁶ instruments which were also used in the Stardust observation campaign. Figure 12 shows the SLIT spectrum and the extrapolation of the thermal emission into the VIS-NIR range and the Echelle data at an altitude of 69.7 km. Upper and lower margins for the thermal emission for a temperature difference of ± 50 K are added. Note that the analysis of the SLIT

data was performed independently from those of the other instruments, and no scaling factors were transferred. The consistency between the independent experiments is what gives confidence in the measured data.

The temperature extraction procedure was carried out for the most intense spectra and temperatures were achieved over altitude for the two cases of constant SRC temperature and linearized distribution. Figure 13 shows a comparison with the results obtained with DPLR, again with averaged and locally resolved temperature. The CFD temperatures for the averaged temperature assumption are in good agreement with the SLIT results except for the values where the tracking was apparently off (shown as open symbols). If a temperature distribution is introduced, the DPLR peak values at the SRC tip are substantially higher by 200 K and more than the experimentally obtained results. However, the experimental method for determining the tip temperatures is consistent with the case of constant temperatures and the results agree with the SLIT and Echelle data.

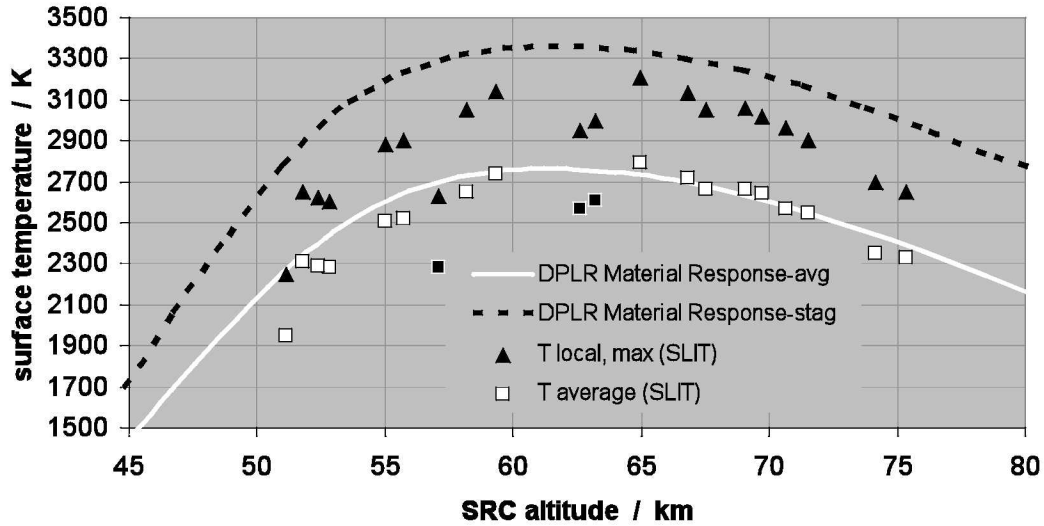


Figure 13. SRC surface temperatures obtained from SLIT emission spectra and DPLR CFD simulations for the assumption of averaged and locally resolved temperatures.

C. Analysis of plasma spectra

The measured spectra were dominated by the emission of CN and N_2^+ . Atomic lines, especially the emission lines of Ca and Ca^+ , were clearly identified in all spectra. There was strong evidence of H and O lines before peak heating, but not after. Lines of N could not be identified clearly. A theoretical simulation of the molecular radiation of CN and N_2^+ was carried out using the line-by-line code EMCAL²⁷ under variation of the rotational and vibrational temperatures between 1000 K and 20000 K. Rotational and vibrational temperatures define the shape of the molecular bands and therefore can be determined without knowing the absolute number densities of electronically excited levels which are most likely in non-equilibrium. The temperatures which originated the best fitting spectra are considered to be the effective rotational and vibrational temperatures. In that sense “effective” shall express the fact that, again, spatial variations of temperature in the post-shock layer have been neglected in this process. In Figure 14 the best fits for the emission of CN Violet and N_2^+ 1st Neg. at altitudes of 77.6 km as one of the first SLIT spectra, 69.7 km in the overlapping regime with Echelle data, 64.9 km as the most reliable spectrum close to peak heating, and 55 km as example after peak heating are shown. The $\Delta v=0$, $\Delta v=1$, and $\Delta v=-1$ bands of both species are clearly visible which enables an extraction of vibrational temperature. In addition, the $\Delta v=-2$ band of N_2^+ is seen. Simulation and measurement show reasonable agreement which improves with decreasing altitude. However, strong scattering is seen in the data, particularly at high altitudes, which might also be emission due to other molecules and atoms which are not yet identified. The formerly reported disagreement between measurement and simulation for the $\Delta v=1$ and $\Delta v=-1$ transitions⁸ vanished after the recalibration procedure described above.

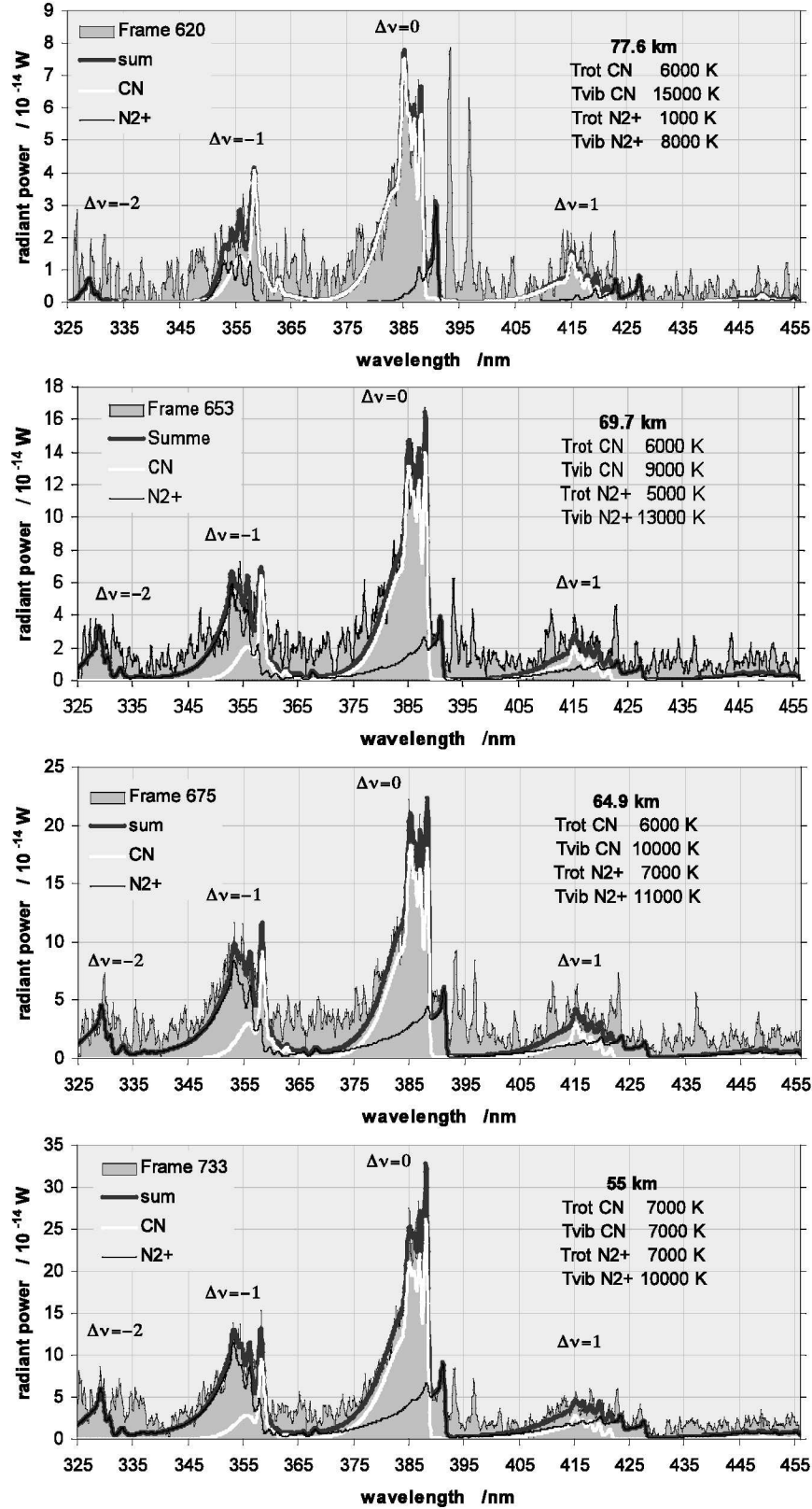


Figure 14. Measured and simulated emission of CN Violet and N₂⁺ 1st Neg. at altitudes of 77.6 km, 69.7 km (comparison with Echelle data), 64.9 km (most reliable spectrum close to peak heating), and 55 km before and after peak heating.

If these fits are applied to all spectra, temperature distributions of N_2^+ and CN can be determined along the trajectory. The vibrational temperature of CN is found to be lower than that of N_2^+ . However, the rotational temperatures are quite close at altitudes below 67 km. In fact, the region with the most effective combination of particle density of the species of concern and underlying temperature will dominate the emitted spectrum. For all measured spectra, CN rotational temperatures are around 7000 K. This temperature is clearly higher than the plasma temperature in the boundary layer close to the surface. CN that is produced close to the surface would have to diffuse through the boundary layer into the post shock region in a sufficient amount to generate molecular emission at the deduced rotational temperatures. Another possibility is that particles from micro-spallation of the heat shield might penetrate the post-shock region. Thus, CN would be produced in the hot region by erosion of these particles yielding emission at the observed temperatures. Further work is needed to check these assumptions. N_2^+ is mainly formed in the post shock layer. This means that the major contributions for the different radiating species in the same spectrum may be produced in different regions of the flow field. Due to the integration over the whole flow field, the temperatures values have probably only limited relevance. However, they are necessary to compute the integrated value of the radiance emitted by the 1st Neg. systems of CN and N_2^+ as the integral of the simulated spectra in the detected wavelength range divided by the corresponding solid angle. A direct integration over experimental spectra would not allow for a separation of these systems. Furthermore, issues with a superposition of other radiating species would introduce new errors. The integral value over the simulated radiation as shown in Fig. 15 might be easier to handle for further analysis using CFD simulation than the single spectra. Compensating curves are plotted for both species to illustrate the general characteristic with SRC altitude. Values which were clearly below these compensating curves are marked by open symbols and are only displayed for the sake of completeness. The scatter in the values is clearly related to the overall intensity on the CCD and therefore to errors in tracking. In addition, predicted radiative and convective (divided by 10 for better visibility) heat fluxes²² are plotted. Both N_2^+ and CN emission seem to reach maximum before peak heating, although reliable data points are available only shortly before and after peak heating. The time history of the N_2^+ emission follows the predicted radiative heat flux quite well. The trend CN emission compared to its peak value is clearly higher than the corresponding value of the radiative heat flux before peak heating and resembles more the convective heat flux history although shifted to higher altitudes. However, after peak heating, the CN emission decreases as quickly as the N_2^+ emission and the predicted radiative heat flux.

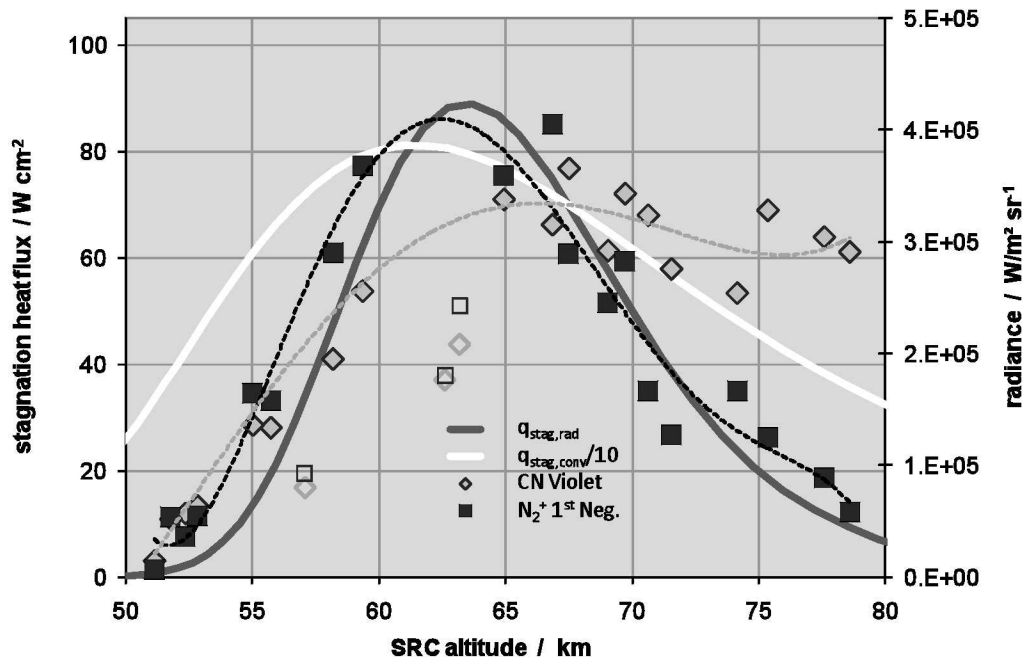


Figure 15. Spatially integrated, emitted radiance of the 1st Neg. system of N_2^+ and the CN Violet integrated in the wavelength range between 325 nm and 456 nm and predicted radiative and convective stagnation heat fluxes²² versus SRC altitude.

One possible interpretation is that in early re-entry, CN emission is mainly determined by ablation while after peak heating, CN emission is dominated by the plasma properties. If this means that at that point CN is mainly generated in the hot plasma region, as it would be if CN were generated by particles that spall from the heat shield, is not clear yet. For further interpretation, a spectral simulation should be performed on the basis of spatially-resolved CFD results. A confirmation of this assumption would entail comparison with measured spectra. However, such a spectral simulation with PARADE²⁸ based on URANUS²⁹ CFD computations of the flow field around Stardust did not show satisfying results mainly due to the fact that the two strongest radiators CN and N_2^+ were either not present in the flow field solver or existed only in very low concentrations yielding a high factor of uncertainty. At present, no reliable alternative is available that would take account of the special variation of temperatures and particle densities in the flow field. Recent predictions³⁰ of the plasma properties show some promise. These simulations might be the basis for more accurate data evaluation.

VI. Summary and Conclusions

The emission of post shock and surface radiation during the Stardust re-entry was detected during a NASA-led mission aboard the Agency's DC-8 airborne observatory. Spectra were taken in the wavelength range from 324 nm to 456 nm with a pixel resolution of 0.08 nm, and with a measurement frequency of 5 Hz during 30 s around the point of maximum heating. Due to the difficulties in tracking, not every spectrum contained data. Nevertheless, the emission of CN as a major ablation product as well as N_2^+ and different atoms could be monitored successfully during that time. Due to the nature of the set up, no spatial resolution of the radiation data was achieved. Therefore, all measured values represent an integration both over the visible part of the glowing heat shield and over the plasma in the post shock region. The measured spectra could be split up into continuum spectra, which represent a superposition of the heat shield radiation and the continuum radiation of potential dust particles in the plasma, and into line spectra from the plasma in the post shock layer. Influence of scattered light during the calibration measurements was significant and corrected for by a recalibration. From the continuum spectra, Planck temperatures were determined under the assumption of constant SRC surface temperatures, and for a temperature distribution whose shape was approximated to a CFD solution with DPLR. The orientation of the SRC relative to the DC8 yielding information on the visible surface and viewing factors as well as the varying distance and atmospheric transmission were taken into account. So far, contributions of glowing dust particles in the surrounding plasma are not included yet. The key results are:

- Intensity corrected emission spectra provide a data basis along the trajectory at altitudes from 77km to 52km. The good agreement with data obtained independently from the Echelle spectrometer in the same observation campaign enhances confidence in both SLIT data acquisition and analysis.
- SRC heat shield temperatures deduced from the experimental data (assuming constant temperatures across the heat shield surface) are in good agreement with results from DPLR CFD analysis. The extrapolation of the thermal radiation to Echelle wavelengths yields error estimates on the order of $\pm 50K$. If a temperature distribution is assumed, the peak temperatures from the experimental data are constantly lower by about 200 K than the corresponding CFD results.
- Rotational temperatures of N_2^+ and CN were obtained from a scaled comparison with simulated spectra. However, these temperatures are only averaged values over the whole flow field. Therefore, they were only used for the computation of spectrally integrated emission of these two species. The time history of the emitted radiance of the N_2^+ 1st Neg. system agrees quite well with the predictions of radiative stagnation heat flux. CN emission at high altitudes, in reference to its peak emission, is stronger and resembles the time evolution of convective heat flux. A possible conclusion is that CN emission is characteristic for surface ablation in early re-entry while it might be dominated by plasma characteristics after peak heating. This emission may be used for a future comparison with CFD data.

Further interpretation of measured emission spectra would require flow field solutions which include ablation products (in particular CN) coupled to a radiation code. Thus, more accurate comparisons with the experimental data should be possible through an integration over the spatially-resolved CFD data. For future missions, a simultaneous optical measurement of plasma properties through on board instrumentation in combination with an airborne observation is proposed to enhance the accuracy of the results by providing additional information on spatial distributions.

Acknowledgments

Preparation of the measurement campaign and first evaluation took place at the Institut für Raumfahrtssysteme of the Universität Stuttgart. The authors wish to thank all IRS members who were involved, in particular, Georg Herdich for preparation of the mission and for tracking, as well as Markus Pietras, Ricarda Wernitz, and Haida Abdennabi for contributions during conception and first evaluation, and Thiemo Knigge and Maria von Schönermark for providing the ModTran data. The authors wish to acknowledge the German Aerospace Center (DLR) and the *Steinbeis Transferzentrum Plasma- und Raumfahrttechnologie* for funding the development of SLIT and the observation itself, and to LOT Oriel/Andor for providing the EMCCD camera. Furthermore, the authors also wish to thank NASA for the opportunity to participate in this mission, as well as for the Group Achievement Award of the NASA Engineering and Safety Center which was presented to the Stardust Hypervelocity Entry Observing Campaign Team. The whole mission would not have been possible without the support of the ground crew at NASA Ames or without the great performance of the DC-8 crew. Thanks also to SETI and Peter Jenniskens for the coordination of the mission. Finally, thanks to Dinesh Prabhu, ELORET Corporation for discussion and comments.

References

- ¹Desai, P.N.; Mitcheltree, R.A.; Cheatwood, F. McNeil, "Entry Trajectory Issues for the Stardust Sample Return Capsule," *International Symposium on Atmospheric Reentry Vehicles and Systems*, Arcachon, France, March 16-18, 1999.
- ²"Stardust Hypervelocity Entry Observing Campaign Support," NASA Engineering and Safety Center Report, RP-06-80, August 31, 2006.
- ³Jenniskens P., Kontinos D., Jordan D., Wright M., Olejniczak J., Raiche G., Wercinski P., Desai P.N., Taylor M.J., Stenbaek-Nielsen H.C., McHarg M.G., Abe S., Rairden R.L., Albers J., Winter M., Harms F., Wolf J., ReVelle D.O., Gural P., Dantowitz R., Rietmeijer F., Hladiuk D., Hildebrand A.R., "Preparing for the meteoric return of Stardust," *Workshop on Dust in Planetary Systems* (ESA SP-643). 26-30 September 2005, Kauai, Hawaii.
- ⁴Jenniskens, P.; Jordan, D.; Kontinos, D.; Wright, M.; Olejniczak, J.; Raiche, G.; Wercinski, P.; Schilling, E.; Taylor, M.; Rairden, R.; Stenbaek-Nielsen, H.; McHarg, M. G.; Abe, S.; Winter, M., "Preliminary Results From Observing The Fast Stardust Sample Return Capsule Entry In Earth's Atmosphere On January 15, 2006," *Progress in Planetary Exploration Missions, 26th meeting of the IAU*, Joint Discussion 10, 21-22 August 2006, Prague, Czech Republic
- ⁵G. A. Raiche. D. M., "Shock Layer Optical Attenuation and Emission Spectroscopy Measurements during Arc Jet Testing with Ablating Models," AIAA 2004-825, *proceedings of the 42th AIAA Aerospace Sciences Meeting and Exhibit*, 5-8 January 2004, Reno, NV.
- ⁶C. Park, G. A. Raiche. D. M., "Radiation of Spalled Particles in Shock Layers," AIAA 2004-1349, *proceedings of the 42th AIAA Aerospace Sciences Meeting and Exhibit*, 5-8 January 2004, Reno, NV.
- ⁷Data sheet for the EMCCD camera DU971N: http://www.lot-oriel.com/site/site_down/cc_du971n_deen03.pdf.
- ⁸Michael Winter and Georg Herdich, "Spectroscopic Observation of the Stardust Re-Entry in the Near UV," AIAA-2007-4050, *39th AIAA Thermophysics Conference*, Miami, FL, 25-28 June 2007.
- ⁹Bernstein, L.S., A. Berk, P.K. Acharya, D.C. Robertson, G.P. Anderson, J.H. Chetwynd and L.M. Kimball, "Very Narrow Band Model Calculations of Atmospheric Fluxes and Cooling Rates," *Journal of Atmospheric Sciences*, Vol. 53, No. 19, pp. 2887-2904, 1996.
- ¹⁰Anderson, G. P., A. Berk, P. K. Acharya, M. W. Matthew, L. S. Bernstein, J. H. Chetwynd, H. Dothe, S. M. Adler-Golden, A. J. Ratkowski, G. W. Felde, J. A. Gardner, M. L. Hoke, S. C. Richtsmeier, B. Pukall, J. Mello and L. S. Jeong, "MODTRAN4: Radiative Transfer Modeling for Remote Sensing," in *Algorithms for Multispectral, Hyperspectral, and Ultraspectral Imagery VI*, Sylvia S. Chen, Michael R. Descour, Editors, Proceedings of SPIE Vol. 4049, pg. 176-183, 2000.
- ¹¹MacCormack, R. and Candler, G., "The Solution of the Navier-Stokes Equations Using Gauss-Seidel Line Relaxation," *Computers and Fluids*, Vol. 17, No. 1, 1989, pp. 135-150.
- ¹²Yee, H., "A Class of High-Resolution Explicit and Implicit Shock Capturing Methods," NASA TM 101088, Feb. 1989.
- ¹³Millikan, R. and White, D., "Systematics of Vibrational Relaxation," *Journal of Chemical Physics*, Vol. 39, No. 12, 1963, pp. 3209-3213.
- ¹⁴Park, C., "Nonequilibrium Hypersonic Aerothermodynamics," Wiley, New York, 1990.
- ¹⁵Parker, J. G., "Rotational and Vibrational Relaxation in Diatomic Gases," *Physics of Fluids*, Vol. 2, 1959, pp. 449-462.

¹⁶ Gupta, R., Yos, J., Thompson, R., and Lee, K., "A Review of Reaction Rates and Thermodynamic and Transport Properties for an 11-Species Air Model for Chemical and Thermal Nonequilibrium Calculations to 30000 K," NASA RP-1232, Aug. 1990.

¹⁷ Bartlett, E.P., Kendal, R.M., and Rindal, R.A., "An Analysis of the Coupled Chemically Reacting Boundary Layer and Charring Ablator: Part IV – A Unified Approximation for Mixture Transport Properties for Multi-component Boundary-Layer Applications," NASA CR-1063, June 1968.

¹⁸ Hirschfelder, J.O., Curtiss, C.F., Bird, R.B., "Molecular Theory of Gases and Liquids," John Wiley and Sons, Inc., 1964.

¹⁹ Desai, P., Qualls, G., and Levit, C., "Stardust Entry Reconstruction," AIAA-2008-1198, Reno, NV, January 2008.

²⁰ F.S. Milos, Y.-K. Chen and T.H. Squire, "Updated Ablation And Thermal Response Program For Spacecraft Heatshield Analysis," Paper TFAWS06-1008, *The 17th Thermal and Fluids Analysis Workshop*, University of Maryland, August 2006.

²¹ F.S. Milos and Y.-K. Chen, "Two-Dimensional Ablation, Thermal Response and Sizing Program for Charring Ablators," AIAA paper 2008-1223, *46th AIAA Aerospace Sciences Meeting*, January 2008.

²² Liu, Y., Prabhu, D., Trumble, K., Saunders, D., Jenniskens, P., "Radiation Modeling For the Reentry of the Stardust Sample Return Capsule," AIAA-2008-1213, Reno, NV, January 2008.

²³ Olynick, D., Chen, Y.K., and Tauber, M.E., "Aerothermodynamics of the Stardust Sample Return Capsule," *Journal of Spacecraft and Rockets*, Vol. 36, No. 3, May-June 1999.

²⁴ Huy K. Tran, Christine E. Johnson, Daniel J. Rasky and Frank C. Hui, Ames Research Center, Moffett Field, California; Ming-Ta Hsu, Tomothy Chen and H.C. Chem, San Jose, California; Y.K. Chen, Thermosciences Institute, Moffett Field, California; Daniel Paragas and Loreeen Kobayashi, Foothill-De Anza College, Cupertino, California, "Phenolic Impregnated Carbon Ablators (PICA) as Thermal Protection Systems for Discovery Missions," NASA Technical Memorandum 110440, Ames Research Center, Moffett Field, California 94035-1000, April 1997.

²⁵ Peter Jenniskens, Michael A. Wilson, Christophe O. Laux and Michael Winter, "High resolution spectroscopy of the Stardust Sample Return Capsule Entry at peak heating with ASTRO," *J. Space Rockets* (this issue).

²⁶ Jenniskens, P., "Observations of the Stardust Sample Return Capsule Entry with a Slit-less Echelle Spectrograph," *J. Space Rockets* (this issue).

²⁷ Winter, M., "Emission Spectroscopic Investigation of the Flow Field around a Blunt Body in a High Enthalpy Flow," Dissertation (in German), Universität Stuttgart, Stuttgart, Germany, Dec. 2006.

²⁸ Winter, M., Pfeiffer, B., Fertig, M., Auweter-Kurtz, M., Smith, A. J., "Recent Status of the Plasma Radiation Database PARADE," AIAA-2004-2376, *proceedings of the AIAA Thermophysics Conference*, USA, Portland, Oregon, 2004.

²⁹ Fertig, M., Dohr, A., Frühauf, H.-H., "Transport Coefficients for High Temperature Nonequilibrium Air Flows," *AIAA Journal of Thermophysics and Heat Transfer*, Vol.15, No.2, 2001.

³⁰ T. Ozawa, J. Zhong, D. A. Levin, D. Bogerz and M. Wright, "Modeling of the Stardust Reentry Flows with Ionization in DSMC," *proceedings of the 45th AIAA Aerospace Sciences Meeting and Exhibit*, 9-12 January 2007, Reno, NV